Ru–W Pair Sites Enabling the Ensemble Catalysis for Efficient Hydrogen Evolution

Weilong Ma, Xiaoyu Yang, Dingding Li, Ruixin Xu, Liangpeng Nie, Baoping Zhang, Yi Wang, Shuang Wang, Gang Wang, Jinxiang Diao, et al.

Ru-W Pair Sites Enabling the Ensemble Catalysis for Efficient Hydrogen Evolution

Weilong Ma, Xiaoyu Yang, Dingding Li, Ruixin Xu, Liangpeng Nie, Baoping Zhang, Yi Wang, Shuang Wang, Gang Wang, Jinxiang Diao, Lirong Zheng, Jinbo Bai, Kunyue Leng, Xiaolin Li* and Yunteng Qu**

W. Ma and X. Yang contributed equally to this work

W. Ma, D. Li, R. Xu, L. Nie, B. Zhang, Y. Wang, S. Wang, G. Wang, K. Leng, Y. Qu
International Collaborative Center on Photoelectric Technology and Nano Functional Materials, Institute of Photonics and Photon-Technology, Northwest University.
Xi'an, Shaanxi 710069, China
lengky@neu.edu.cn; yuntengqu@nwu.edu.cn

X. Yang
Oncology Department, National Clinical Research Center for Geriatric Disorders, Xiangya Hospital, Central South University.
Changsha, 410083, China

J. Diao
Aeronautical Polytechnic Institute.
Xi’ an, 710089, China

L. Zheng
Institute of High Energy Physics.
Beijing 100039, China

J. Bai
Université Paris-Saclay, CentraleSupélec, ENS Paris-Saclay, CNRS, LMPS-Laboratoire de Mécanique Paris-Saclay.
8-10 rue Joliot-Curie, Gif-sur-Yvette 91190, France

X. Li
Institute of Intelligent Manufacturing Technology, Shenzhen Polytechnic.

Shenzhen 518055, China
E-mail: lixiaolin0427@szpt.edu.cn

Keywords: Ru-W pair site, optimizing elementary steps, Ru single-atom, efficient hydrogen evolution

Simultaneously optimizing elementary steps such as water dissociation, hydroxyl transferring, and hydrogen combination is crucial yet challenging for efficient hydrogen evolution reaction (HER) in alkaline media. Herein, we developed Ru single atom-doped WO_2 nanoparticles with atomically dispersed Ru-W pair sites (Ru-W/WO_2) through a crystalline lattice-confined strategy for efficient alkaline HER. It was found that Ru-W/WO_2 exhibited remarkable HER activity with a low potential (11 mV at 10 mA cm^{-2}), notable mass activity (5863 mA mg^{-1}Ru at 50 mV), as well as robust stability (500 h at 250 mA cm^{-2}). The highly efficient activity of Ru-W/WO_2 stem from the synergistic effect of Ru-W sites through ensemble catalysis, in which the W sites expedite rapid hydroxy transferring and water dissociation, and the Ru sites accelerate the hydrogen combination process, synergistically facilitating the HER activity. This study opens a promising pathway for tailoring the coordination environment of atomic-scale catalysts to achieve efficient electrocatalysis.

1. Introduction

Water electrolysis powered by sustainable electricity offers a cost-effective and readily available approach for producing green hydrogen, and is considered a key element in achieving future carbon neutrality.[1-3] The hydrogen evolution reaction (HER) plays a pivotal role in water electrolysis, but the use of noble-based anode catalysts and expensive proton exchange membranes in acidic electrolytes has prompted the search for efficient alkaline HER electrocatalysts.[4-5] Recently, platinum (Pt) based materials are considered the benchmark and most capable electrocatalysts for HER, but their scarcity poses significant limitations for practical applications,[6] Ruthenium (Ru) as one of the platinum-group metals is identifying as an ideal alternative for developing efficient HER catalysts.[7] However, the strong interaction of hydrogen and hydroxyl species over Ru species hinders further water dissociation, hydrogen desorption, and combination processes, resulting in unsatisfactory HER performance.[8] Therefore, there is a pressing need to selectively tailor the electronic structure of Ru to fine-tune the adsorption and desorption abilities of hydrogen and hydroxyl species in a controlled manner, but still challenging.

Single atom catalysts (SACs) with tunable local coordination environment represent a promising material platform for modulating the electronic structures of active sites,[9,10] as demonstrated by their ability to optimize the free energy of intermediates during the HER process.[11] Currently, various Ru SACs have been developed by modulating anions ligands in the first coordination shell, resulting in excellent alkaline HER activity, such as Ru SAs@PN,[12] Ru-MoS_2/CC,[13] R-NiRu,[14] RuSA–$Ti_3C_2T_x$,[15] etc. In these cases, the anions ligands surrounding the Ru site regulate the strong adsorption of hydrogen on Ru, promoting H desorption and combination. However, these isolated Ru sites still exhibit strong hydroxyl adsorption,[8,16] as the single active sites are unable to break the scaling relation.[17,18] Recently, tailoring the coordination fields through cation regulation has been shown to efficiently improve catalytic activity, particularly for complex multistep reactions.[19,20] Electro-catalysts

containing paired metal sites offer significant potential to precisely design the active moiety for regulating the binding energy of multiple intermediates simultaneously,[21-22] which is advantageous for alkaline HER but has been rarely investigated.

Inspired by the pioneering works exploiting W as regulator for Ru nanoparticles,[23-26] we employ a lattice-confined strategy to construct Ru-W/WO_2-800 catalysts with well-defined Ru-W pair sites through cation replacement. XAFS and STEM analyses confirm that Ru atoms are embedded into the crystalline lattice of WO_2 and strongly bonded with adjacent W atoms. The optimized catalyst exhibits remarkable activity for HER in alkaline media, with a low overpotential of only 11 mV at 10 mA cm^{-2}, high mass activity of 3829 mA mg^{-1}Ru at 50 mV, and robust stability up to 500 hours at 250 mA cm^{-2}. Operando electrochemical Raman measurements, combined with theoretical calculation, reveal that the superior activity of Ru-W/WO_2-800 derive from the synergistic effect of Ru-W pair sites through ensemble catalysis. Specifically, the W sites facilitate rapid hydroxyl transfer and water dissociation, while the Ru sites accelerate the hydrogen combination process, synergistically enhancing the HER activity.

2. Results and Discussion

2.1. Ru-W pair catalysts synthesis.

Figure S1 (Supporting Information) illustrate the synthetic process of the Ru-W pair doped WO_2. Typically, dopamine hydrochloride is firstly mixed with $RuCl_3$ in acidic solution, then Na_2WO_4 is added to gain spherical polydopamine-based metal-organic compounds (Figure S2 and S3, Supporting Information). After annealing in inert atmosphere at 800 ℃, Ru-W/WO_2-800 with Ru-W dual sites on tungsten oxide is obtained (Figure 1a). In order to investigate the pivotal role of the Ru-W pair in Ru-W/WO_2-800, single atom Ru supported on WO_2 (Ru_1/WO_2-800) is prepared as comparison (Figure S4, Supporting Information). Furthermore, nitrogen-coordinated single atom Ru (Ru SACs, Figure S5, Supporting Information), commercial Ru/C, commercial Pt/C and tungsten oxide (WO_2-800, Figure S6, Supporting Information) are also used as references.

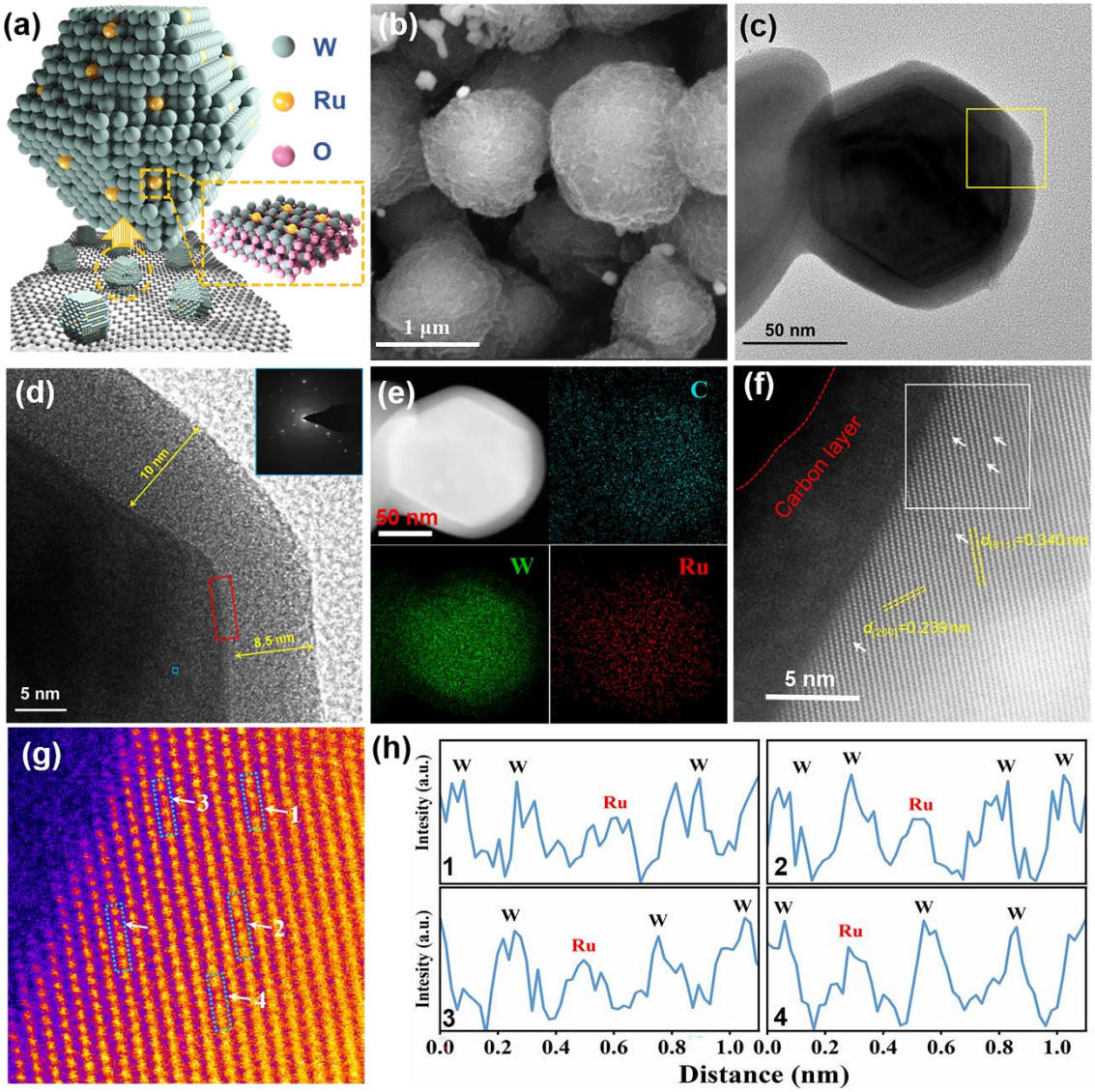

106

107 **Figure 1.** (a) Simulative structure and (b) SEM image of Ru-W/WO_2-800. (c, d) TEM images
108 and (e) EDS element mapping of a well-crystallized WO_2 in Ru-W/WO_2-800. (f, g) HAADF-
109 STEM images of the atom arrays of the WO_2 crystal and the surface Ru-W atom pairs. (h)
110 Line intensity profiles along the (011) plane in g.

111 **2.2. Physical characterization.**

112 The element mapping results of Ru-W/WO_2-800 indicate the existence and the uniform
113 distribution of W and Ru over carbon substrate (Figure S7, Supporting Information). The
114 corresponding W and Ru contents are confirmed as 25 wt% and 1.3 wt% by ICP (Table S1,
115 Supporting Information), respectively. Figure 1b displays the SEM images of Ru-W/WO_2-800,
116 which reveals a spherical morphology consisted by the aggregation of nano flakes. The TEM
117 image further confirms the randomly dispersion of WO_2 particles and nano clusters in the

agminated flakes (Figure S8, Supporting Information). Considering the insufficient ability of single atom Ru or W dopped carbon in HER,[26,27] the potential active sites for HER are mainly concentrate on the well-crystallized WO_2 particles in Ru-W/WO_2-800. As shown in Figure 1c, the WO_2 crystal takes a hexagonal morphology, a carbon layer about 8-10 nm is observed enveloping the WO_2 (Figure 1d), which may help promoting its stability. The EDS element mapping confirms the carbon enveloping and the uniform distribution of Ru on WO_2 particle Figure 1e). The aberration-corrected HAADF-STEM is employed to study the surface structure of the WO_2 particle. As shown in Figure 1f, W atomic array with lattice spacing of 0.239 and 0.340 nm are clearly observed, which correspond to the (200) and (011) plane of the monoclinic WO_2. Moreover, some dark atomic columns are observed inserting in the W atomic array randomly, which could be distinguished as Ru atom on the surface of WO_2 (Figure 1g). Line profiles of the HAADF-STEM are taken around Ru atom along the (011) plane, the variable atomic column intensity in Figure 1h demonstrating the replacement of lattice W atom by Ru atom. Moreover, the Ru sites doping in WO_2 lattice are also distinguished on the WO_2 clusters in Ru-W/WO_2-800 (Figure S9, Supporting Information). For Ru_1/WO_2-800, the HAADF-STEM image reveals the WO_2 atom array and dark atomic columns of Ru (Figure S10, Supporting Information), and the distortion of atom array around Ru atom. However, whether the Ru in Ru_1/WO_2-800 and Ru-W/WO_2-800 manifest as Ru single atom or Ru-W coordination still need be further distinguished by spectral investigations.

Figure 2a show the XRD pattern of Ru doped WO_2 catalysts, both Ru-W/WO_2-800 and Ru_1/WO_2-800 display the diffraction peaks belonging to (011), (200), (-202), (-220) and (310) planes of monoclinic WO_2 at 25.9°, 36.7°, 37.5°, 53.3° and 60.0°, and the peaks of crystalline Ru is absent. To further distinguish the Ru and W combination in Ru-W/WO_2-800 and Ru_1/WO_2-800, the X-ray adsorption fine spectroscopy (XAFS) are exploited. The oxidation state of W in Ru-W/WO_2-800, Ru_1/WO_2-800 and WO_2-800 are confirmed similar based on

the W L_3-edge XANES spectra (Figure 2b), which approximate to +4, consisting with the W 4f

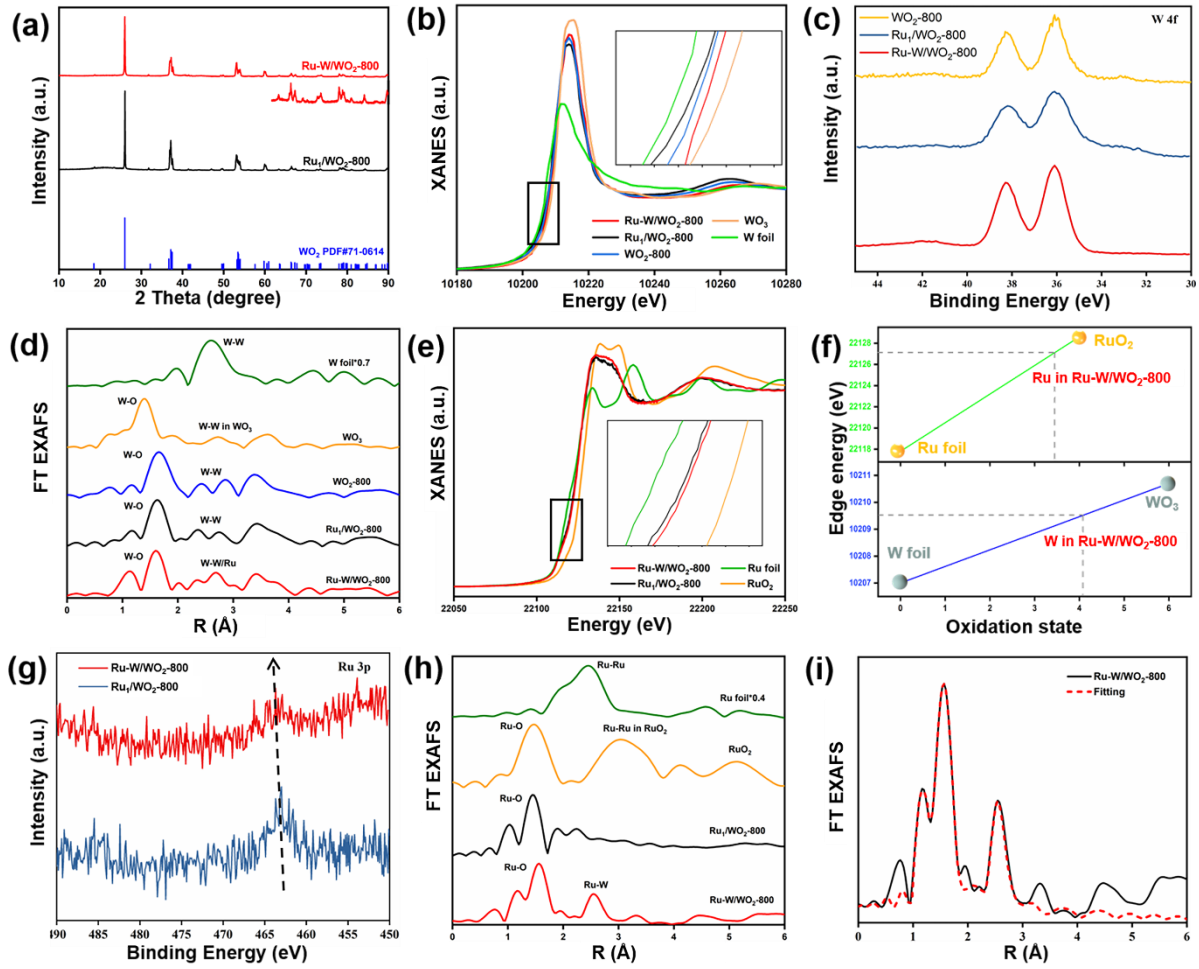

Figure 2. Coordination environment of Ru-W/WO_2-800 and Ru_1/WO_2-800. (a) XRD patterns. (b) W L_3-edge XANES spectra. (c) W 4f XPS spectra. (d) W L_3-edge edge FT EXAFS spectra. (e) Ru *K*-edge XANES spectra. (f) The simulative oxidation state of Ru and W in Ru-W/WO_2-800. (g) Ru 3p XPS spectra. (h) Ru *K*-edge FT EXAFS spectra. (i) FT EXAFS fitting curve of Ru-W/WO_2-800 at R space.

XPS spectra (Figure 2c).[28] The W L_3-edge FT EXAFS spectra are shown in Figure 2d, the differences of the secondary coordination between Ru-W/WO_2-800, Ru_1/WO_2-800 and WO_2-800 suggesting the disturbance of W-W coordination in Ru-W/WO_2-800 induced by the Ru inserting. To further reveal the interaction of the Ru-W pair in Ru-W/WO_2-800, the Ru K-edge XAS are taken in reference to Ru_1/WO_2-800, Ru foil and RuO_2. Figure 2e shows the Ru K-edge XANES. According to the location of white-line intensity of Ru-W/WO_2-800, which between that of Ru foil and RuO_2, the oxidative state of Ru in Ru-W/WO_2-800 is indicated

between 0 and +4. The linear simulation of edge energy and oxidation state is practiced in Figure 2f. The fitting result discloses that the average oxidation state of Ru in Ru-W/WO_2-800 is +3.4, slightly higher than the +3.3 in Ru_1/WO_2-800 (Figure S11, Supporting Information), in line with the Ru 3p XPS spectra (Figure 2g).[29] The Ru K-edge FT EXAFAS of Ru-W/WO_2-800 displays a dominant peak at ~1.5 Å (Figure 2h), which belonging to the Ru-O coordination. Moreover, the secondary peak at ~2.5 Å demonstrates the existence Ru-W coordination, which is larger than the Ru-Ru bonding in Ru foil (~2.4 Å), due to relatively bigger atomic diameter of W. Figure 2i and Table S2(Supporting Information) give the Ru K-edge EXAFS fitting results of Ru-W/WO_2-800. The coordination number of Ru-O bonding and Ru-W bonding are simulated as 3.1 and 0.9, respectively, indicating the formation of Ru-W dual atom sites, which embedding into the lattice of WO_2 crystalline. For Ru_1/WO_2-800, only a dominant peak at ~1.5 Å is observed in the Ru K-edge EXAFS, the absence of Ru-Ru and Ru-W coordination confirm the Ru single atom are absorbed onto the surface of WO_2.

2.3. Electrocatalytic performance evaluation.

The synergistic effect of the Ru-W bonding should be benefit for the boosting of the hydrogen evolution process. Thus, we employ the three-electrode system to evaluate the HER performance of Ru-W/WO_2-800, in reference to Ru_1/WO_2-800, WO_2-800, Ru SACs, commercial Ru/C and Pt/C. Figure 3a show the linear sweep voltammetry (LSV) curves in 1 M KOH, in which the Ru-W/WO_2-800 displays a remarkable onset potential that near zero. A significant reduced overpotential of 11 mV (at 10 mA cm^{-2}) is confirmed over Ru-W/WO_2-800 (Figure S12, Supporting Information), lower than that over Pt/C, Ru/C, Ru_1/WO_2-800, Ru SACs and WO_2-800, demonstrating its superior HER performance. Moreover, Ru-W/WO_2-800 also reveals a low potential of 152 mV to gain a current density of 1 A cm^{-2} (Figure S13). The insufficient activity of WO_2-800 indicates the dominant of Ru in actuating the HER

process. Furthermore, the relatively higher overpotential of Ru_1/WO_2-800 compared to that of Ru-W/WO_2-800 reveal the pivotal role of Ru-W bonding for boosting the HER pathway.

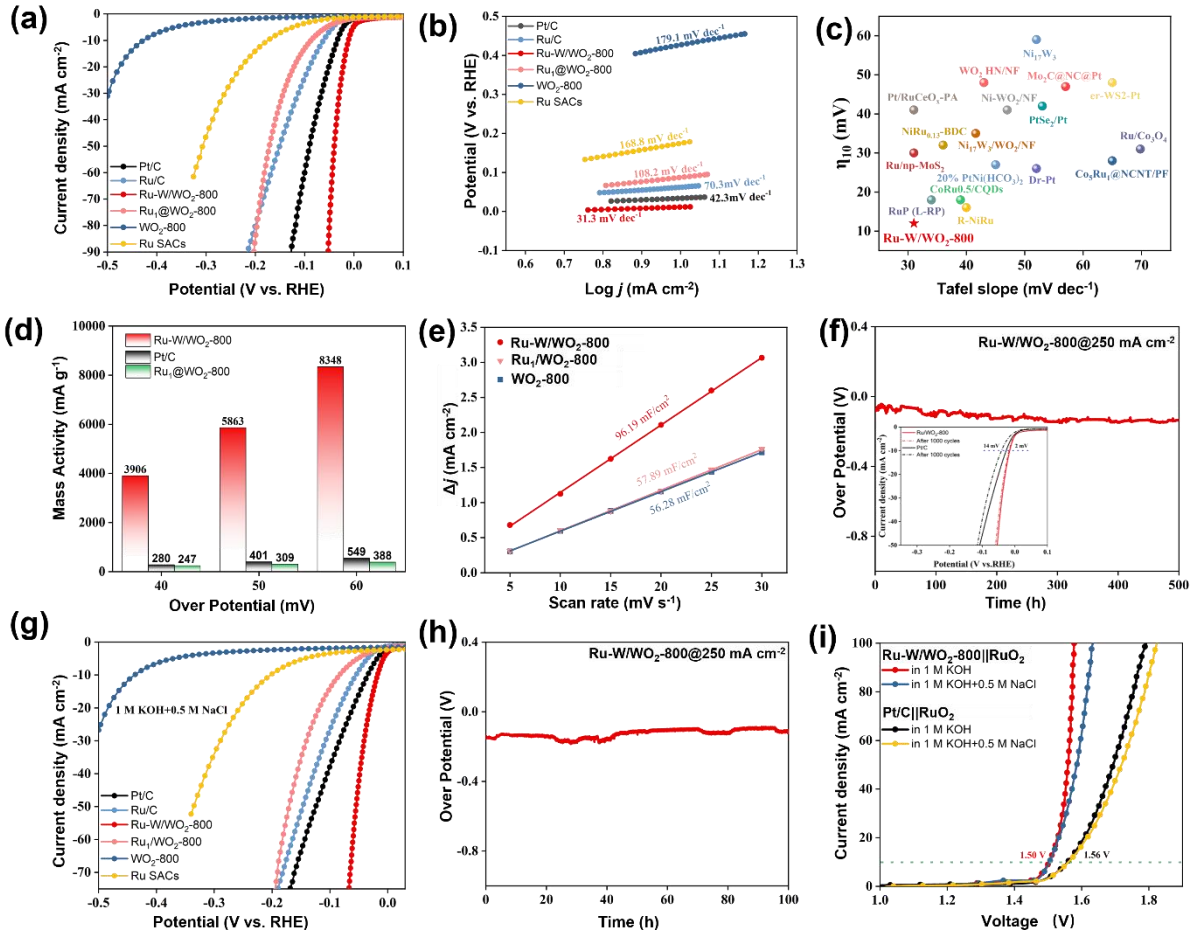

Figure 3. HER evaluation in alkaline medium. (a) Linear sweep voltammetry (LSV) curves and (b) Tafel plots of Ru-W/WO_2-800 and reference catalysts. (c) Comparison of the HER performance between Ru-W/WO_2-800 and other reported catalysts. (d) Mass activity of Ru-W/WO_2-800, Ru_1/WO_2-800 and Pt/C. (e) The current density differences vs. scan rate and the corresponding yielded C_{dl} for Ru-W/WO_2-800, Ru_1/WO_2-800 and WO_2-800. (f) Chronopotentiometry test at 250 mA cm^{-2} and the LSV curve of Ru-W/WO_2-800 before and after 1000 cycles (insert) in 1 M KOH. (g) LSV curves in alkaline simulated seawater of 1 M KOH and 0.5 M NaCl. (h) Chronopotentiometry test at 250 mA cm^{-2} of Ru-W/WO_2-800 in alkaline simulated seawater. (i) Overall water-splitting performance of the Ru-W/WO_2-800||RuO_2 and Pt/C||RuO_2 electrode couples.

The much lower Tafel slope of Ru-W/WO_2-800 (31.3 mV dec^{-1}) further demonstrate its outstanding HER activity (Figure 3b), even compared with the previously reported works (Figure 3c). This observation can be attributed to the high intrinsic HER activity of Ru-W/WO_2-800, which is further confirmed by its notably turnover frequency (Figure S14,

Supporting Information). Figure 3d show the normalized activity based on the mass of metal, Ru-W/WO_2-800 exhibits a mass activity of 5863 mA mg^{-1}Ru at 50 mV, over 14 times higher than that of Pt/C (401 mA mg^{-1}Pt), suggesting its larger application potential. The larger double-layer capacitances (C_{dl}) of Ru-W/WO2-800 than that of Ru_1/WO_2-800 (Figure 3e and Figure S15, Supporting Information), combining with the smaller charge transfer resistance (Figure S16, Supporting Information), further demonstrating the evident advantage of the synergistic Ru-W pair sites. Figure 3f present the stability tests. The robustness of Ru-W/WO_2-800 is confirmed by the negligible increasing of the overpotential after 1000 cycles and the superior long-term stability of Ru-W/WO_2-800 up to 500 h at 250 mA cm^{-2}. Furthermore, the used Ru-W/WO_2-800 maintained its original structure, revealing the good structure stability (Figure S17, Supporting Information).

Electrochemical hydrogen production exploiting seawater is drawing great attention recently, due to the huge reserves of the feedstock.[30,31] Thus, the hydrogen generation ability of electrocatalysts in alkaline simulated seawater (1 M KOH and 0.5 M NaCl) are tested. As shown in Figure 3g and Figure S18 (Supporting Information), although all catalysts display a decline in the HER activity compared with that in alkaline fresh water, the Ru-W/WO_2-800 still exhibit a sufficient overpotential of 22 mV at 10 mA cm^{-2} and a Tafel slope of 33.8 mV dec^{-1}. The robustness of the Ru-W/WO_2-800 in alkaline simulated seawater is also confirmed by the chronopotentiometry test at 250 mA cm^{-2} up to 100 h (Figure 3h). Inspiring by the excellent HER performance of Ru-W/WO_2-800 in both alkaline freshwater and alkaline simulated seawater, the overall water-splitting is measured due to its significant application.[32-35] The electrolyzer is assembled by using Ru-W/WO_2-800 as cathode and commercial RuO_2 as anode (Ru-W/WO_2-800 || RuO_2 couple), and in reference to Pt/C || RuO_2 couple. As shown in Figure 3i, the Ru-W/WO_2-800 || RuO_2 couple just require 1.50 mV to gain a current density of 10 mA cm^{-2} in 1 M KOH, lower than the 1.56 mV of Pt/C || RuO_2 couple. Moreover, the current density over Ru-W/WO_2-800 || RuO_2 couple was much higher

compare with that over Pt/C || RuO_2 couple at large voltages. The water-splitting ability of Ru-W/WO_2-800 in seawater is also evaluated, in agreement with the LSV curve in Figure 3g, a slight decline of the activity is observed due to the obstruction of active sites by the NaCl, but its current density is still higher than that of Pt/C. The water splitting performance demonstrate the application potential of Ru-W/WO_2-800 as cathode material for producing green hydrogen by water electrolysis.

2.4. Understanding the active sites.

To clarify the HRE process, potential dependent operando Raman spectroscopy are conducted in both H_2O and D_2O solution of 1 M KOH. The operando Raman spectra of Ru-W/WO_2-800 are recorded at the potential from -0.7 to -1.2 V (vs. Ag/AgCl), which shifts from the non-Faradaic region to the HER region. Figure 4a shows the Raman spectra of Ru-W/WO_2-800 in the 1 M KOH solution of H_2O. The signal at 798 cm^{-1} and 1634 cm^{-1} should belong to the W-O in WO_2 and H-O-H bending mode of water.[36-38] Moreover, a new signal emerges at 884 cm^{-1} when negative shift the potential to -1.0 (vs. Ag/AgCl), the intensity of which increases after further shift the potential to 1.2 (vs. Ag/AgCl). As reported, this signal may be attributed to the Ru-H stretch.[23] To clarify the attribution of the Raman signal at 884 cm^{-1}, 1 M KOH solution of D_2O is used. As shown in Figure 4b, after H_2O is changed to D_2O, the signal at 884 cm^{-1} shifts to 614 cm^{-1}, the downward shift ratio is estimated as 69.5%, close to the theoretical 71.1%, which confirm the Ru-H stretch on Ru-W/WO_2-800. Considering the Ru-H stretch emerges at a potential as low as -1.0 (vs. Ag/AgCl), efficient water dissociation is demonstrated for Ru-W/WO_2-800.

DFT calculations are used to further dig the original effect of the Ru-W synergy on the HER pathway. A model with bonded Ru-W pair in cell of WO_2 is constructed based on the experimental results of Ru-W/WO_2-800 (Figure 4c). For comparison, the model of Ru adsorbed on the surface of WO_2 (Ru_1/WO_2-800), pure WO_2 (WO_2-800) and N-coordinated Ru single atom (Ru SACs) are also built (Figure S19, Supporting Information). The OH_{ad}

poisoning effect is firstly investigated by the absorption energy of OH_{ad} ($E_{abs}OH$). As shown in Figure 4d and Figure S20 (Supporting Information), the Ru site in Ru-W/WO_2-800 exhibits a $E_{abs}OH$ of -0.421 eV, higher than that of Ru site in Ru_1/WO_2-800 (-0.632 eV) and Ru site in Ru SACs (-0.632 eV), suggesting the weakening of Ru-OH interaction by Ru-W pair. Moreover, the strong interactions of W-OH on W site in Ru-W/WO_2-800 and W site in WO_2-800 further demonstrate the optimizing of the OH absorption over Ru-W dual atom sites in Ru-W/WO_2-800.

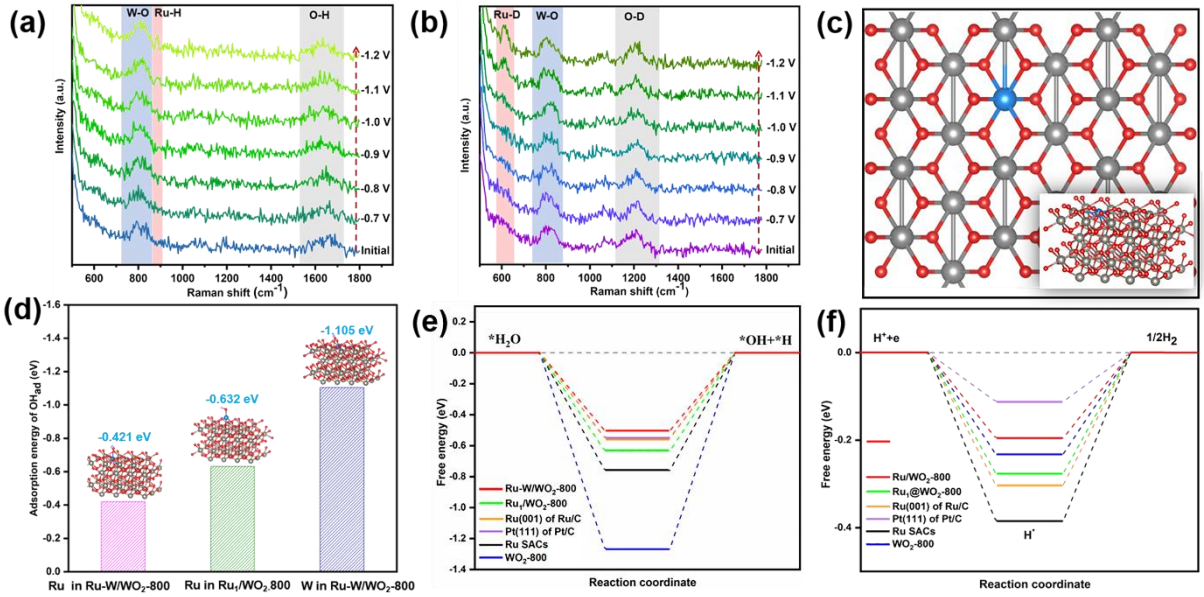

Figure 4. (a, b) Operando Raman spectra of Ru-W/WO_2-800 at different potential vs. Ag/AgCl in 1 M KOH in H_2O (a) and D_2O (b). (c) Simulative structure of Ru-W/WO_2-800. (d) Simulative OH adsorption model and corresponding adsorption energy on Ru and W sites. (e) Free energy diagram for water dissociation. (f) Free energy diagram for hydrogen recombination.

Figure S21 (Supporting Information) presents the absorption energy of H_2O ($E_{abs}H_2O$), which disclosed the faster H_2O capture on the Ru site in Ru-W/WO_2-800 ($E_{abs}H_2O$=-1.325 mV) compared with that on Ru_1/WO_2-800 and Ru SACs, suggesting the acceleration of the following H_2O dissociation step. The optimal water dissociation intermediate (H-OH) on Ru-W/WO_2-800 is demonstrated in Figure S22 (Supporting Information) as the *H absorbing on Ru site and *OH absorbing on the bonded W site. Based on this optimal structure, Ru-W/WO_2-800 displays the lowest H_2O dissociation barrier of 0.50 eV compared with Ru single

atom, Pt/C and Ru/C (Figure 4e), indicating its best H_2O dissociation ability. Furthermore, the optimized the hydrogen recombination ability of Ru-W/WO_2-800 in alkaline medium is also revealed by the DFT calculations (Figure 4f and Figure S23, Supporting Information). Overall, compared with the adsorbed Ru on WO_2 in Ru_1/WO_2-800, the bonded Ru-W dual atom site in the WO_2 lattice gives Ru-W/WO_2-800 the solid advantages of: (1) rapid hydroxy transferring performance, (2) superior H_2O dissociation ability, (3) optimized the hydrogen recombination. Thus, the HER performance of Ru/WO_2-800 in alkaline medium is significant boosted by the synergistic effect of the Ru-W dual atom sites.

3. Conclusion

In this work, we fabricated a Ru single atom doped WO_2 by lattice confined strategy, which was identified as bonded Ru-W pairs embedding in the lattice of well-crystallized WO_2. The resultant Ru-W/WO_2-800 delivered excellent HER performance under alkaline and seawater media with ultralow overpotential and remarkable mass activity, as well as robust stability at high current density. Moreover, the Ru-W/WO_2-800 also presented low voltages in overall water splitting system, beneficial for practical application. The DFT calculation combining with the operando Raman spectra revealed that the outstanding HER activity stems from the synergetic effect of Ru-W pair sites via an ensemble catalysis, in which the W sites expedite the rapid hydroxy transferring and water dissociation, the Ru sites accelerate the hydrogen combination process. This work may provide important inspire for designing atomic-scale catalysts aiming at complicated electrocatalysis.

Supporting Information

Supporting Information is available from the Wiley Online Library or from the author.

Acknowledgements

We thank the photoemission endstation beamline 1W1B station in the Beijing Synchrotron Radiation Facility (BSRF) for help with the characterizations. This work is financially supported by the National Natural Science Foundation of China (22275147, 21902150), Natural Science Basic Research Program of Shaanxi (2022JQ-082 and 2022JM-018) and China Postdoctoral Science Foundation (2020M673461).

Conflict of Interest

The authors declare no Conflict of Interest.

Author contributions

K.L. and Y.Q. designed and wrote this work. J.B. and X.L. supervised and funded this work. W.M. conducted the catalysts synthesis and the HER evolutions. X.Y., D.L., R.X., L.N. and L.Z. gave their helps in the characterizations. P.B. and S.W designed and practiced the operando Raman measurements. Y.W., G.W. and J.D. co-modified the paper. All authors revised the writing work of this study.

Received: ((will be filled in by the editorial staff))
Revised: ((will be filled in by the editorial staff))
Published online: ((will be filled in by the editorial staff))

References

[1] B. E. Logan, L. Shi, R. Rossi, *Joule*. **2021**, *5*, 752-767.

[2] J. Liu, X. Meng, J. Xie, B. Liu, B. Tang, R. Wang, C. Wang, P. Gu, Y, Song, S. Huo, J. Zou, *Adv. Funct. Mater.* **2023**, 2300579.

[3] J. Liu, J. Xie, R. Wang, B. Liu, X. Meng, X. Xu, B. Tang, Z. Cai, J. Zou, *Chem. Eng. J.* **2022**, *450*, 137961.

[4] X. Wang, Y. Zheng, W. Sheng, Z. J. Xu, M. Jaroniec, S. Qiao, *Mater. Today*. **2020**, *36*, 125-138.

[5] S. Anantharaj, S. Noda, V. R. Jothi, S. Yi, M. Driess, P. W. Menezes. *Angew. Chem. Int. Ed.* **2021**, *60*, 18981-19006.

[6] Y. Liu, Q. Wang, J. Zhang, J. Ding, Y. Cheng, T. Wang, J. Li, F. Hu, H. Yang, B. Liu. *Adv. Energy. Mater.* **2022**, *12*, 2200928.

[7] J. Jiao, N,-N. Zhang, C. Zhang, N. Sun, Y. Pan, C. Chen, J. Li, M. Tan, R. Cui, Z. Shi, J. Zhang, H. Xiao, T. Lu, *Adv. Sci*. **2022**, *9*, 2200010.

[8] J. Zhang, G. Chen, Q. Liu, C. Fan, D. Sun, Y.Tang, H. Sun, X. Feng, *Angew. Chem. Int. Ed.* **2022**, *61*, e202209486.

[9] W. Ma, Z. Deng, X. Zhang, Z. Zhang, Z. Zhou, *J. Mater. Chem. A.* **2023**;

[10] Y. Jia, Z. Xue, J.Yang, Q. Liu, J. Xian, Y. Zhong, Y. Sun, X. Zhang, Q. Liu, D. Yao, G. Li, *Angew. Chem. Int. Ed.* **2022**, *61*, e202110838.

[11] T. Ma, H. Cao, S. Li, S. Cao, Z. Zhao, Z. Wu, R. Yan, C. Yang, Y. Wang, P. A. Aken, L. Qiu, Y.-G. Wang, C. Cheng, *Adv. Mater*. **2022**, *34*, e2206368.

[12] J. Yang, B. Cheng, X. Liu, W. Liu, Z. Li, J. Dong, W. Chen, W. Yan, T. Yao, X. Duan, Y. Wu, Y. Li, *Angew. Chem. Int. Ed.* **2018**, *57*, 9495-9500.

[13] D. Wang, Q. Li, C. Han, Z. Xing, X. Yang, *Appl. Catal. B Environ.* **2019**, *249*, 91-97.

[14] X. Chen, J. Wan, J. Wang, Q. Zhang, L. Gu, L. Zheng, N. Wang, R. Yu, *Adv. Mater.* **2021**, *33*, e2104764.

[15] H. Liu, Z. Hu, Q. Liu, P. Sun, Y. Wang, S, Chou, Z. Hu, Z. Zhang, *J. Mater. Chem. A.* **2020**, *8*, 24710-24717.

[16] Q. He, Y. Zhou, H. Shou, X. Wang, P. Zhang, W. Xu, S, Qiao, C. Wu, H. Liu, D. Liu, S. Chen, R. Long, Z. Qi, X. Wu, Li. Song, *Adv.Mater.* **2022**, *34*, e2110604.

[17] X.Zhou, K. Han, K. Li, J. Pan, X.Wang, W. Shi, S. Song, H. Zhang, *Adv.Mater*. **2022**, *34*, 2201856.

[18] L. Ro, J. Qi, S. Lee, M. Xu, X. Yan, Z. Xie, G. Zakem, A. Morales, J. G. Chen, X. Pan, D. G. Vlachos, S. Caratzoulas, P. Christopher, *Nature*. **2022**, *609*, 287-292.

[19] F. -J. Liu, W. -L. Luo, Z. Zhang, J. Yu, J. -X. Cai, Z. -Y. Yang, *Angew. Chem. Int. Ed*. **2022**, *61*, e202205946.

[20] J. Liu, C. Tang, Z. Ke, R. Chen, H. Wang, W. Li, C. Jiang, D. He, G. Wang, X. Xiao. *Adv. Energy. Mater.* **2022**, *12*, 2103310.

[21] P. Zhu, X. Xiong, D. Wang, *Nano Res.* **2022**, *15*, 5792-5815.

[22] X. Zheng, B. Li, Q. Wang, D. Wang, Y. Li, *Nano Res.* **2022**, *15*, 7806-7839.

[23] J. Chen, C. Chen, M. Qin, B. Li, B. Lin, Q. Mao, H. Yang, B. Liu, Y. Wang, *Nat. Commun*. **2022**, *13*, 5382.

[24] Q. Yang, C. Zhang, B. Dong, Y. Cui, F. Wang, J. Cai, P. Jin, L. Feng, *Appl. Catal. B Environ.* **2021**, *296*, 120359.

[25] C. Xie, W. Chen, S. Du, D. Yan, Y. Zhang, J. Chen, B. Liu, S. Wang, *Nano Energy* **2020**, *71*, 104653.

[26] B. Lu, L. Guo, F. Wu, Y. Peng, J. E. Lu, T. J. Smart, N. Wang, Y. Z. Finfrock, D. Morris, P. Zhang, N. Li, P. Gao, Y. Ping, S. Chen, *Nat.Commun*. **2019**, *10*, 631.

[27] W. Chen, J. Pei, C.-T. He, J. Wan, H. Ren, Y. Wang, J. Dong, K, Wu, W.-C. Cheong, J. Mao, X. Zheng, W. Yan, Z. Zhuang, C. Chen, Q. Peng, D. Wang, Y. Li, *Adv. Mater*. **2018**, *30*, e1800396.

[28] S. Li, B. Chen, Y. Wang, M. -Y. Ye, P. A. Aken, C. Cheng, A. Thomas, *Nat.Mater*. **2021**, *20*, 1240-1247.

[29] H. Yin, Z. Chen, Y. Peng, S. Xiong, Y. Li, H. Yamashita, J. Li, *Angew. Chem. Int. Ed.* **2022**, *61*, e202114242.

[30] L. Wu, F. Zhang, S. Song, M. Ning, Q. Zhu, J. Zhou, G. Gao, Z. Chen, Q. Zhou, X. Xing, T. Tong, Y. Yao, J. Bao, L. Yu, S. Chen, Z. Ren, *Adv. Mater.* **2022**, *34*, e2201774.

[31] H. Zhang, J. Diao, M. Ouyang, H. Yadegari, M. Mao, M. Wang, G. Henkelan, F. Xie, D. J. Riley, *ACS. Catal.* **2023**, *13*, 1349-1358.

[32] B. Lin, J. Chen, R. Yang, S. Mao, M. Qin, Y. Wang, *Appl. Catal. B Environ.* **2022**, *316*, 121666.

[33] P. Wang, Y. Luo, G. Zhang, Z. Chen, H. Ranganathan, S. Sun, Z. Shi, *Nano-Micro Lett.* **2022**, *14*, 120.

[34] X. Zheng, M. Qin, S. Ma, Y. Chen, H. Ning, R. Yang, S. Mao, Y. Wang, *Adv. Sci.* **2022**, *9*, 2104636.

[35] V. R. Stamenkovic, D. Strmcnik, P. P. Lopes, N. M. Markovic, *Nat. Mater.* **2017**, *16*, 57-69.

[36] S. Xie, D. Chen, C. Gu, T. Jiang, S. Zeng, Y. Y. Wang, Z. Ni, X. Shen, J. Zhou, ACS. *Appl. Mater. Interfaces*. **2021**, *13*, 33345-33353;

[37] T. Zhang, J. Jin, J. Chen, Y. Fang, X. Han, J. Chen, Y. Li, Y. Wang, J. Liu, L. Wang, *Nat. Commun.* **2022**, *13*, 6875;

[38] Y. -H. Wang, S. Zheng, W. -M. Yang, R. -Y. Zhou, Q. -F. He, P. Radjenovic, J. -C. Dong, S. Li, J. Zheng, Z. -L. Yang, G. Attard, F. Pan, Z. -Q. Tian, J. -F. Li, *Nature.* **2021**, *600*, 81-85.

Atomically dispersed Ru-W pair site doping WO_2 are fabricated as alternative of Pt-based materials for developing efficient alkaline HER catalyst. The synergistic effect of Ru-W sites triggers ensemble catalysis, resulting in superior performance for electrochemical hydrogen generation.

Weilong Ma, Xiaoyu Yang, Dingding Li, Ruixin Xu, Liangpeng Nie, Baoping Zhang, Yi Wang, Shuang Wang, Gang Wang, Jinxiang Diao, Lirong Zheng, Jinbo Bai, Kunyue Leng, Xiaolin Li* and Yunteng Qu**

Ru-W Pair Sites Enabling the Ensemble Catalysis for Efficient Hydrogen Evolution

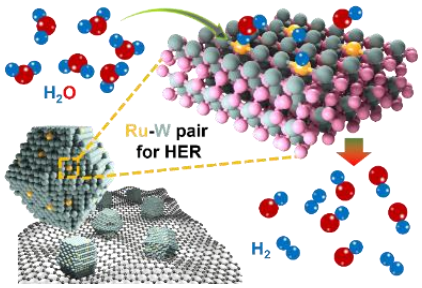

Supporting Information

Ru-W Pair Sites Enabling the Ensemble Catalysis for Efficient Hydrogen Evolution

Weilong Ma, Xiaoyu Yang, Dingding Li, Ruixin Xu, Liangpeng Nie, Baoping Zhang, Yi Wang, Shuang Wang, Gang Wang, Jinxiang Diao, Lirong Zheng, Jinbo Bai, Kunyue Leng, Xiaolin Li* and Yunteng Qu**

Materials and Methods

1.Materials:

All chemicals were analytical grade and without further purification. Analytical grade Sodium tungstate dihydrate,Ruthenium(III) chloride trihydrate, dopamine hydrochloride, Hydrogen chloride and potassium hydroxide were obtained from Innochem. Commercial Pt/C (20 wt%), Ru/C (5 wt%) and Nafion were acquired from Sigma-Aldrich.

2. Synthesis of Ru-W/WO_2-800:

Firstly, 2 mmol of dopamine hydrochloride was dissolved in 20 ml of deionized water, and the pH value was adjusted to 2 by adding 800 μl HCl (1 mol L^{-1}). Then, 0.1 mmol of $RuCl_3$· xH2O was added to the solution and mixed by stirring to obtain a homogeneous solution. After that, 20 ml $Na_2WO_4 \cdot 2H_2O$ solution (0.1 mol L^{-1}) was slowly dropped into the solution under vigorous stirring. A large amount of brown precipitate formed immediately. The reaction was further stirred for 1 h, the obtained product was collected by centrifugation, washed with deionized water and ethanol 3 times. The precursor was dried in an oven at 60 ℃ overnight and heated at 800 ℃ for 2 h in Ar atmosphere at a heating rate of 2 ℃/min.

3. Synthesis of WO_2-800:

WO_2 was prepared without the addition of any other metal salts followed by the same synthetic approach of Ru-W/WO_2-800.

4. Synthesis of Ru_1/WO_2-800:

Firstly, 100 mg WO_2-800 were mixed with 50 mL ethanol and stirred for 0.5 h. After that, 2 mg $RuCl_3$· xH_2O was added in solution and further stirred for 12 h. Then, evaporated the

solvent to dryness at 70 ℃, and kept the obtained sample under Ar atmosphere at 350 ℃ for 2 h.

5. Synthesis of Ru SACs catalysts:

In a typical synthesis, 3 ml NH_4OH, 80ml ethanol and 180ml deionized water were mixed by stirring 10 minutes. Following, 10ml pure dopamine solution (40 mg ml^{-1}) and 10 ml Ru contained dopamine solution (DA=40 mg ml^{-1}, Ru=0.43 mg ml^{-1}) were slowly alternate dropped into the solution under vigorous stirring. The reaction was further stirred for 12 h and gradually formed brown precipitation under stirring. The obtained product was collected by centrifugation, washed with deionized water and ethanol 3 times. The precursor was dried in an oven at 60 ℃ overnight and heated at 800 ℃ for 5 h in Ar atmosphere at a heating rate of 2 ℃/min.

6.Characterization:

Scanning electron microscopy (SEM) images were obtained on a FEI Apreo S microscope. Transmission electron microscopy (TEM) and high-resolution transmission electron microscope (HR-TEM) images were collected with a Talos F200X microscope. Aberration-corrected scanning transmission electron microscopy (AC HAADF-STEM) images were collected with a JEOL JEM-ARM200F microscope. The X−ray diffraction (XRD, Bruker D8 Advance) was used to analyze crystal structures. X-ray photoelectron spectroscopy (XPS) measurements were conducted on a PHI 5000 Verasa spectrometer using Al Kα radiation. The metal contents in the catalysts were determined by Inductively Coupled Plasma Optical Emission Spectrometer (ICP-OES) on a Agilent 5110.X-ray absorption fine structure (XAFS) measurements for the Ru K-edge, W L3-edge were performed on beamline 1W1B of Beijing Synchrotron Radiation Facility. The acquired EXAFS data were extracted and processed according to the standard procedures using the ATHENA module implemented in the IFEFFIT software packages. Operando Raman spectra were measured under controlled electrochemical potentials using a three-electrode epoxy cell with a counter electrode of Pt wire and Ag/AgCl. A controlled active area of 0.384 cm2 by an insulation layer on carbon paper drop-casted with 0.1 mg catalyst was used as the working electrode. Raman spectra were collected using a Raman spectrometer (WITEC Alpha500) by a 633 nm He–Ne laser (Research Electro-Optics, Inc., USA) at the objective. A 20× microscope objective lens (NA=0.4, Epiplan-Neofluar, Zeiss, Germany) was used, focusing on the sample surface and avoiding the contact to the electrolyte. Acquisition time was set as 20 s for the spectral Raman shift ranging from 800 to 1,800 cm-1 window a UHTS300 spectrometer (WITec GmbH,

Germany) with a CCD camera (Andor Tech-nology, UK) operating at -60 °C. The downward shift ratio and the theoretical value was calculated based on the equation below:

$$\gamma = \frac{\nu(\mathrm{RuD})}{\nu(\mathrm{RuH})} = \frac{\sqrt{m(Ru) + m(D)}}{\sqrt{m(Ru) \times m(D)}} \div \frac{\sqrt{m(Ru) + m(H)}}{\sqrt{m(Ru) \times m(H)}}$$

Where γ represents the downward shift ratio, ν represents the Raman shift, m represents the relative molecular mass.

7. Electrochemical measurement:

All the electrochemical measurements were carried out in a conventional three-electrode cell using the CHI 760E electrochemical workstation at room temperature. A rotating disk electrode (RDE) with a glassy carbon (GC) electrode (diameter: 5 mm; area: 0.196 cm^2) was utilized as the working electrode (WE), and the Pt plate was used as the counter electrode. The Ag/AgCl reference electrode calibrated with RHE in 1 M KOH was used as a reference electrode for long-time stability measurement. For electrode preparation,10 mg of Ru-W/WO_2-800 catalyst was dispersed in the mixture solution of IPA (400 μl) and 5 wt.% Nafion (20 μl) by sonication for over 30 minutes. Then,10 μl of the catalyst ink was drop-cast onto the surface of the GC electrode and dried in the air. Linear sweep voltammetry (LSV) plots were carried out in an Ar saturated 1.0 M KOH with a sweep rate of 1 mV s^{-1} at 1600 rpm. All of the potentials in LSV are 100% iR-corrected. The resistance for iR-compensation was tested at the open circuit potential, Ru-W/WO_2-800 (9.3 Ω), Ru_1@WO2-800 (8.3 Ω), Pt/C (8.0 Ω), Ru/C (8.4 Ω), Ru SACs (8.9 Ω) and WO_2-800 (8.3 Ω). All the potentials were converted to the reversible hydrogen electrode (RHE) by equation.

$$V_{RHE}=E_{(VS\ Ag/AgCl)}+0.197+0.0592*pH$$

The Tafel slope was obtained the LSV curve using the equation of η=a+blogj, where a refers to the intercept, b is the Tafel slope and η denotes the overpotential. Electrochemical impedance spectroscopy (EIS) measurements were collected at η=20 mV in the frequency range from 10 kHz to 0.01 Hz, The Mass activity is calculated based on equation of Mass Activity=I/m, where I(A) is the measured current, m (mg) is the mass of Ru loaded on the GC electrode. The turnover frequency (TOF) is calculated based on the equation of TOF=I/(4Fn), where I(A) is the measured current. F is the Faraday constant (96485 C mol^{-1}). n=m/M, n (mol) is the molar amount of Ru loaded on the GC electrode, m is the mass of Ru, and M is the molecule weight. For the double-layer capacitor (C_{dl}) data, cycling voltammetry (CV) curves were recorded in the non-Faradic region with scanning rate of 5,10, 15, 20, 25 and 30

mV s^{-1}, and he C_{dl} can be obtained by plotting the current difference (Δj) against the scanning rate.

8. Computational Method:

We have employed the first-principles to perform density functional theory (DFT) calculations within the generalized gradient approximation (GGA) using the Perdew-Burke-Ernzerhof (PBE) formulation.[1-3] We have chosen the projected augmented wave (PAW) potentials to describe the ionic cores and take valence electrons into account using a plane wave basis set with a kinetic energy cutoff of 520 eV.[4,5] Partial occupancies of the Kohn−Sham orbitals were allowed using the Gaussian smearing method and a width of 0.05 eV. The electronic energy was considered self-consistent when the energy change was smaller than 10^{-5} eV. A geometry optimization was considered convergent when the energy change was smaller than 0.05 eV $Å^{-1}$. In our structure, the U correction is used for W and Ru atoms. The Brillouin zone integration is performed using 2×2×1 Monkhorst-Pack k-point sampling for a structure. Finally, the adsorption energies (E_{ads}) were calculated as $E_{ads}= E_{ad/sub} -E_{ad} -E_{sub}$, where $E_{ad/sub}$, E_{ad}, and E_{sub} are the total energies of the optimized adsorbate/substrate system, the adsorbate in the structure, and the clean substrate, respectively. The free energy was calculated using the equation:

$$G=E_{ads}+ZPE-TS$$

where G, E_{ads}, ZPE and TS are the free energy, total energy from DFT calculations, zero-point energy and entropic contributions, respectively. The U correction for W and Ru were used as 4.18 and 4.92 eV for d orbital, respectively.

Supplementary Figures

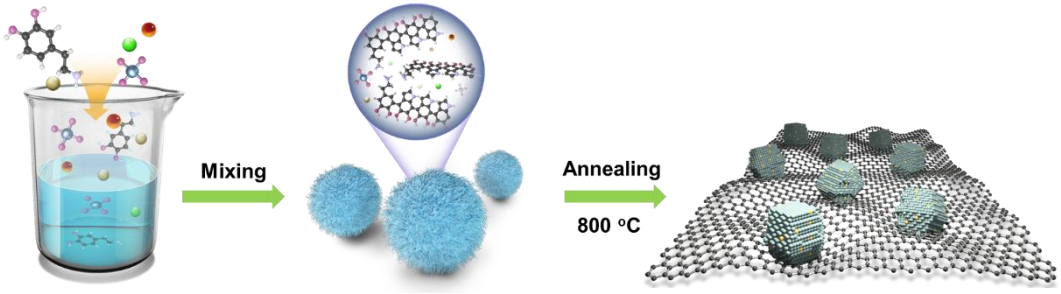

Figure S1. Illustration of the synthetic process of dual-atom Ru-W catalyst.

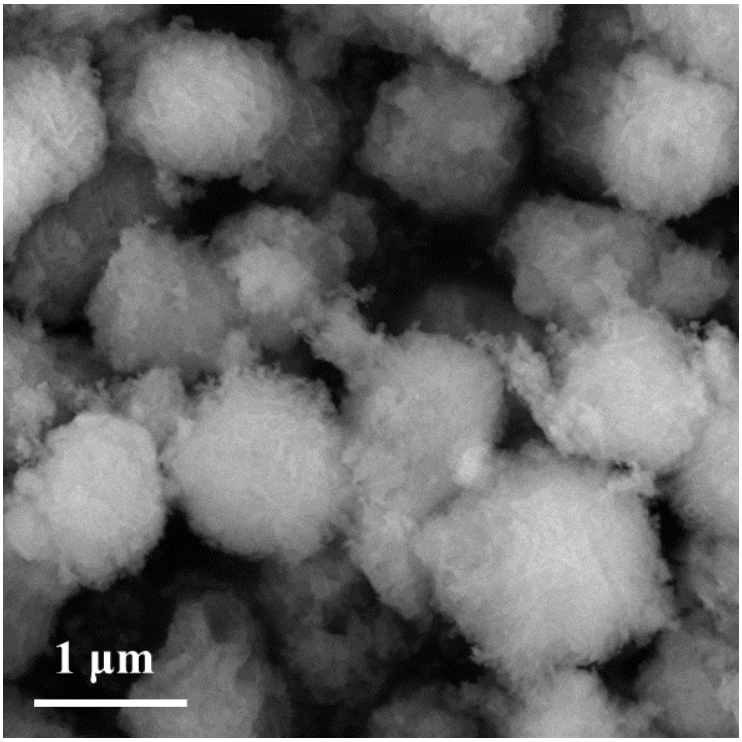

Figure S2. SEM image of as obtained mixture of polydopamine, W and Ru.

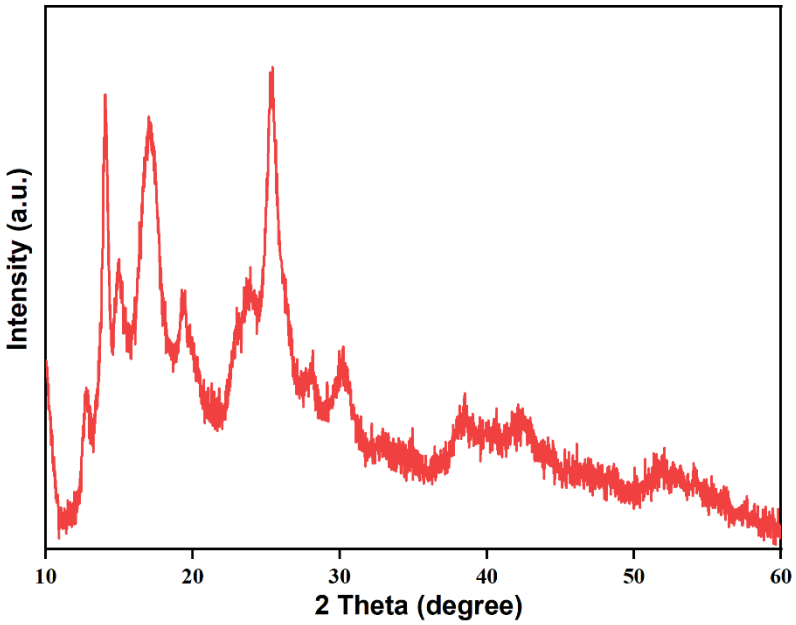

Figure S3. XRD pattern of the as obtained mixture of polydopamine, W and Ru. Only the diffraction peaks belonging to polydopamine were observed.

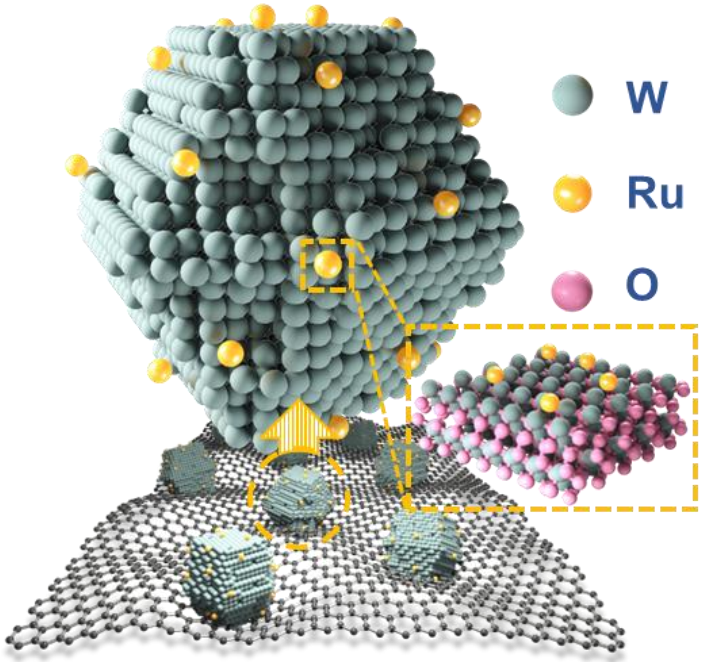

Figure S4. Simulative structure of Ru_1/WO_2-800. Single atom Ru sites randomly disperse on the surface of WO_2.

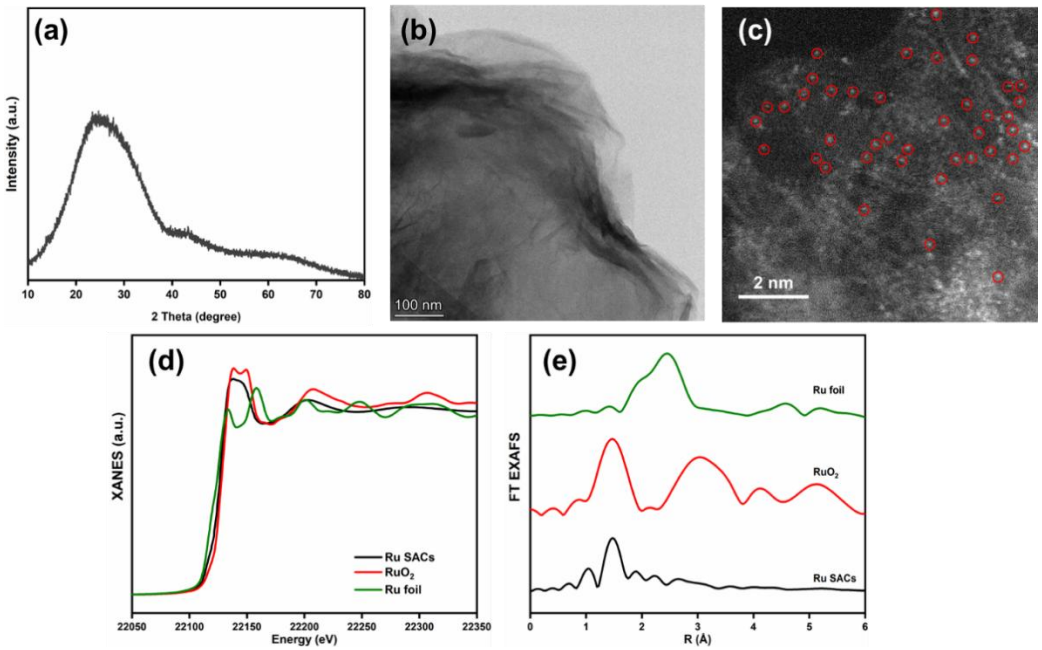

Figure S5. Structure identification of Ru SCAs. (a) XRD pattern, (b) TEM image, (c) Aberration-Corrected HAADF-STEM images, (d) Ru K edge XANES spectrum, (e) Ru K edge FT EXAFS spectrum.

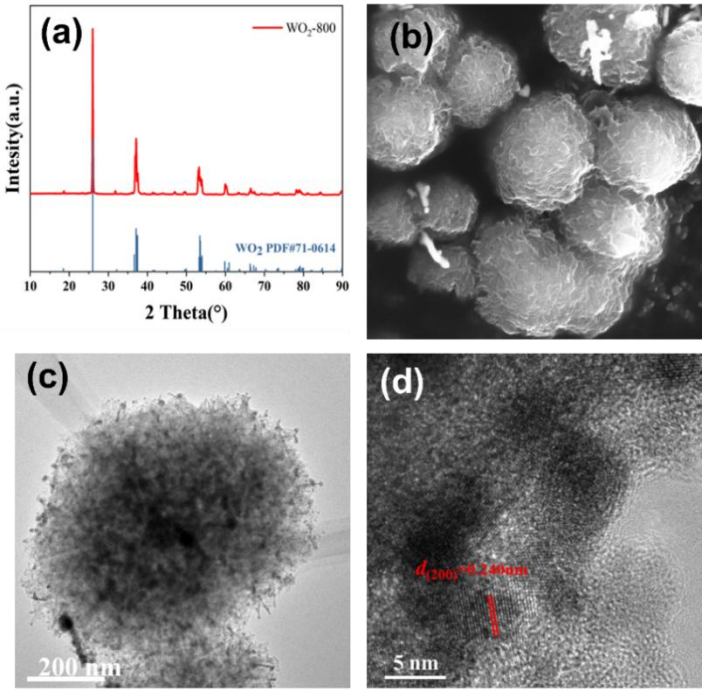

Figure S6. Characterization of WO_2-800. (a) XRD pattern, (b) SEM image, (c) TEM image, (d) HRTEM image.

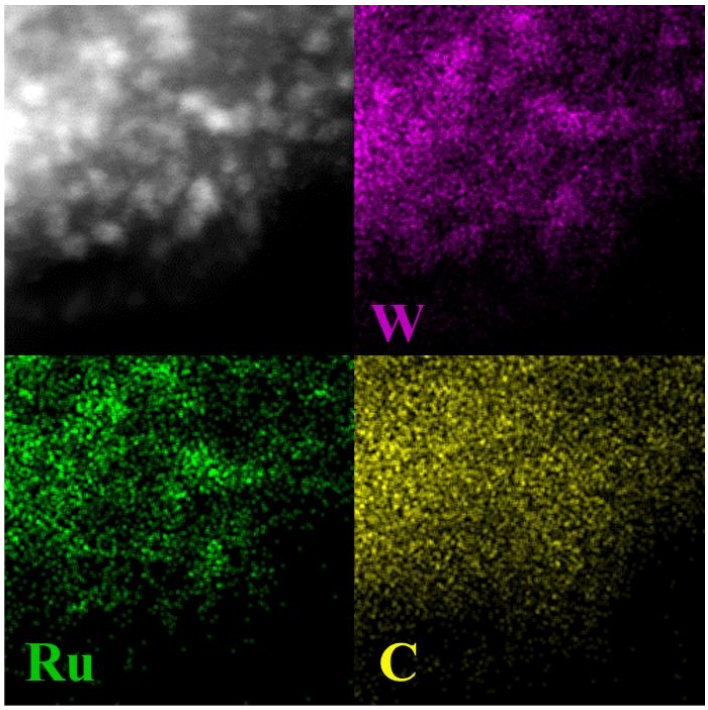

Figure S7. EDS element mapping of Ru-W/WO_2-800.

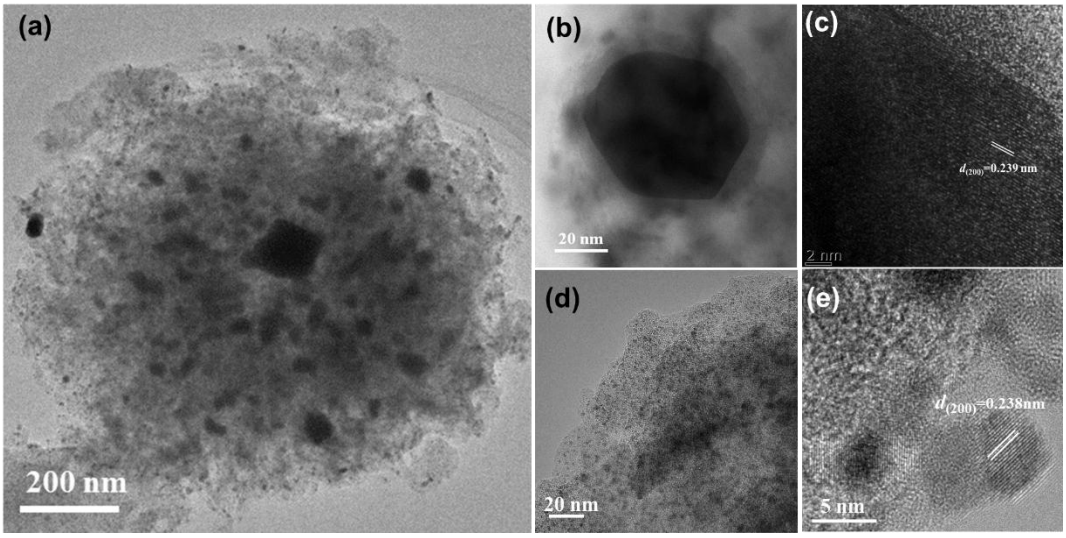

Figure S8. TEM images. (a) Ru-W/WO_2-800. (b, c) WO_2 particle in Ru/WO_2-800. (d, e) WO_2 cluster in Ru/WO_2-800.

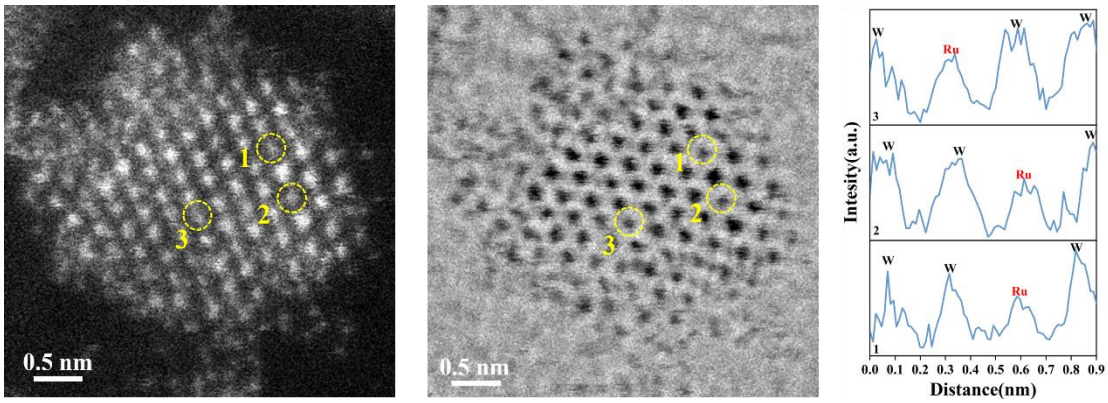

Figure S9. Dark and bright filed STME images and corresponding line intensity profiles of WO_2 clusters in Ru-W/WO_2-800.

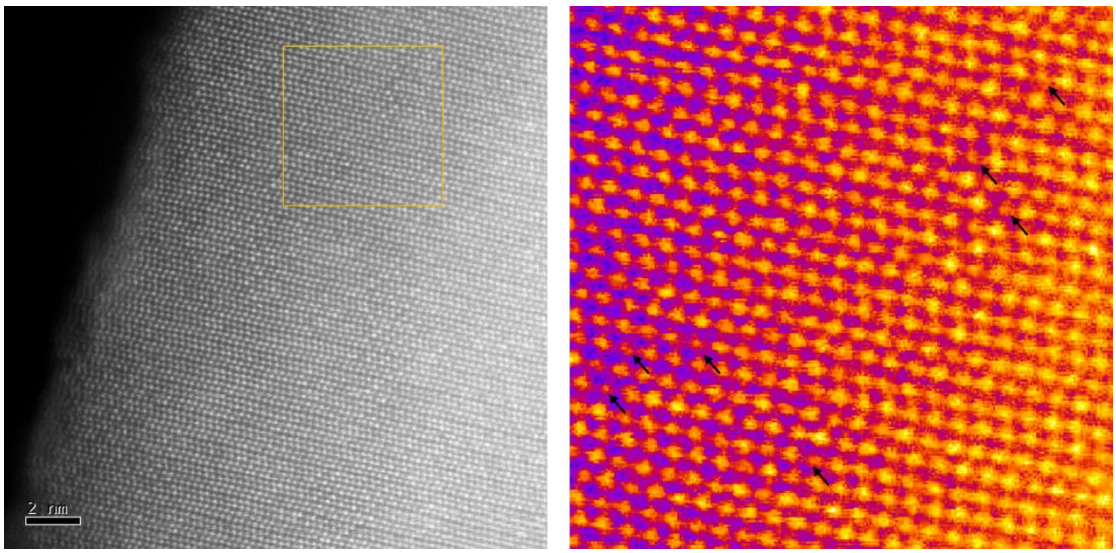

Figure S10. Aberration-Corrected HAADF-STEM images and corresponding intensity profiles of Ru_1/WO_2-800

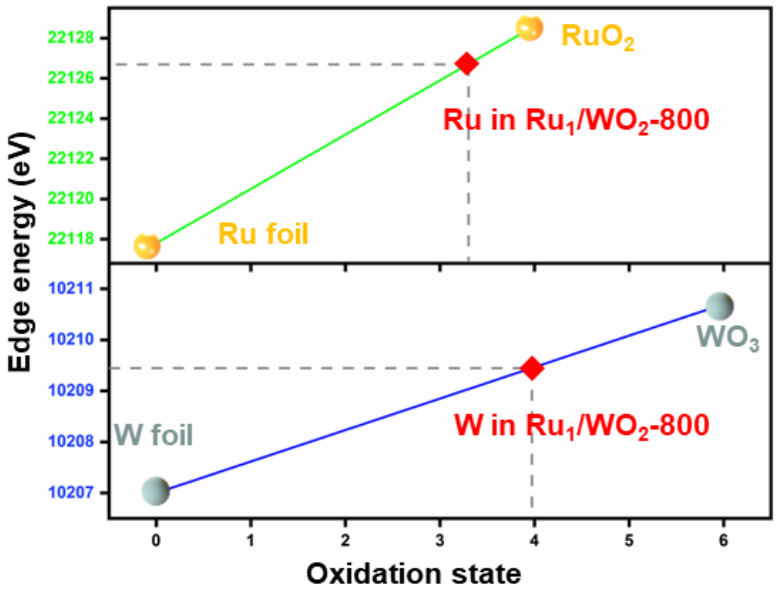

Figure S11. Simulative oxidation state of Ru and W in Ru_1/WO_2-800

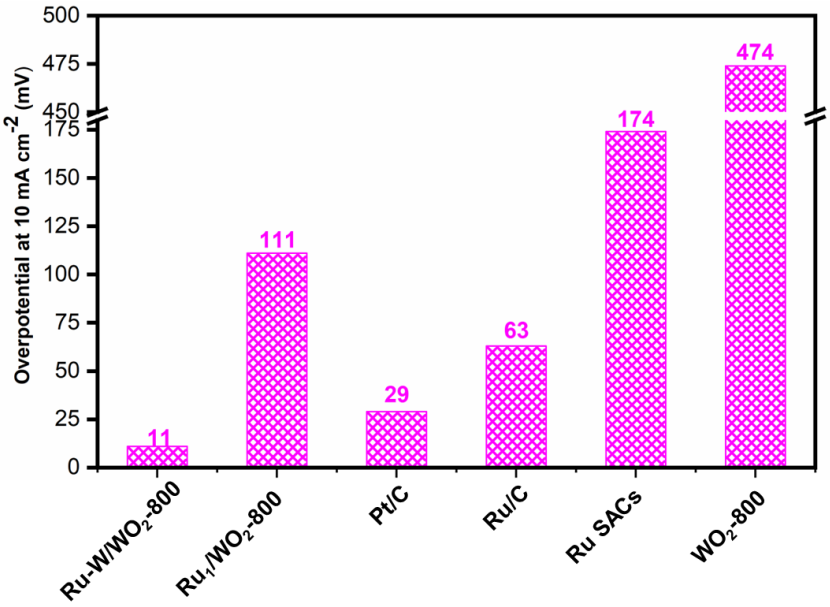

Figure S12. Overpotential of Ru-W/WO_2-800, Ru_1/WO_2-800, Pt/C, Ru/C, Ru SACs and WO_2-800 at a current density of 10 mA cm^{-2}.

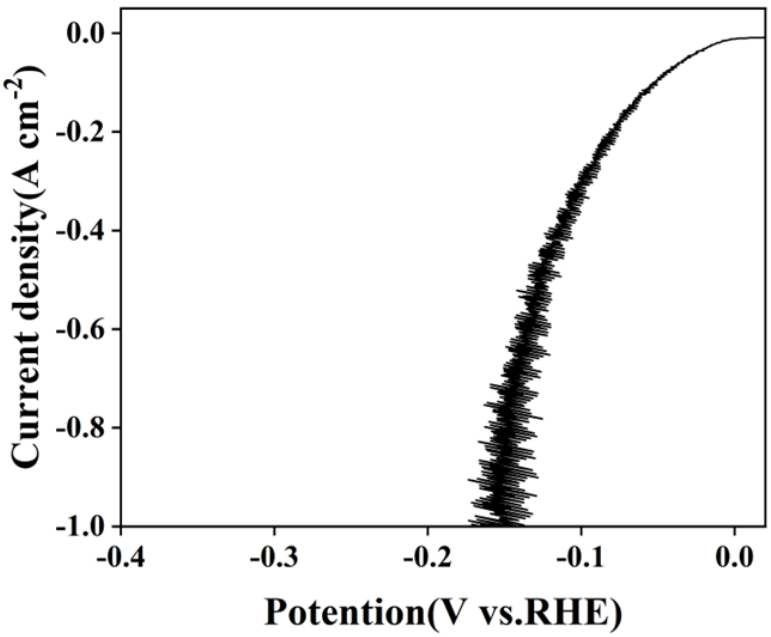

Figure S13. LSV curve of Ru-W/WO_2-800 in 1 M KOH under higher current density.

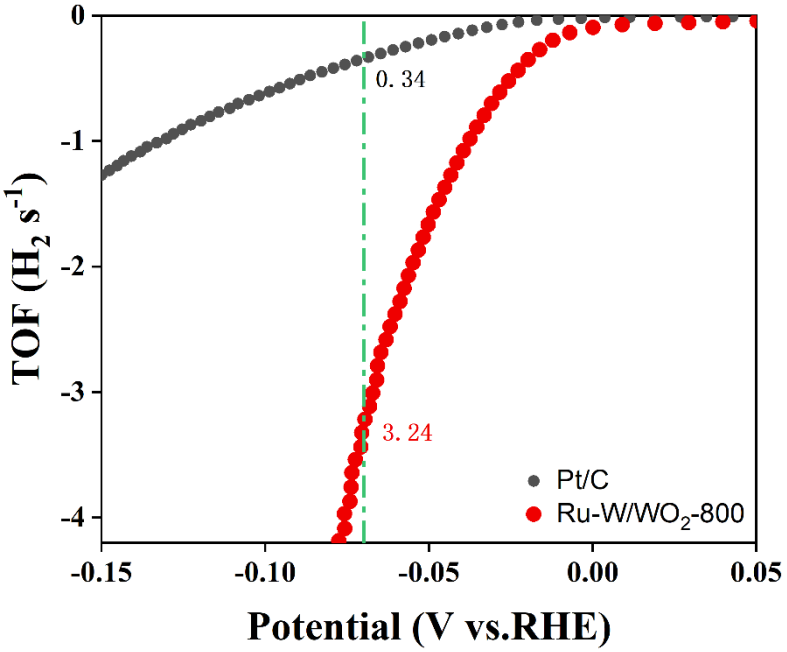

Figure S14. The turnover frequency of Ru-W/WO_2-800 and Pt/C for HRE in 1 M KOH.

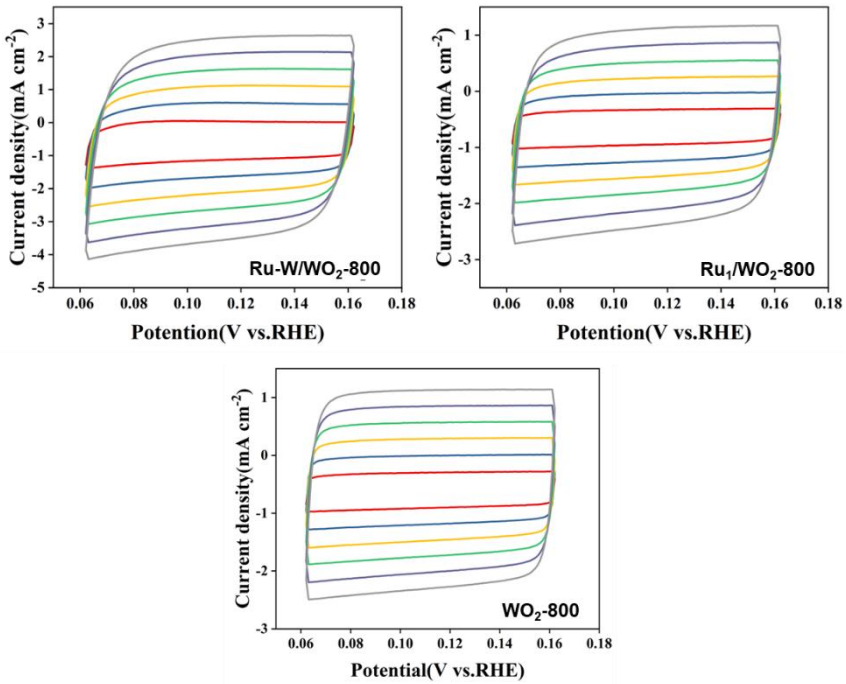

Figure S15. Cyclic voltammetry curves at different scan rates (mV s^{-1}) for Ru-W/WO_2-800, Ru_1/WO_2-800 and WO_2-800.

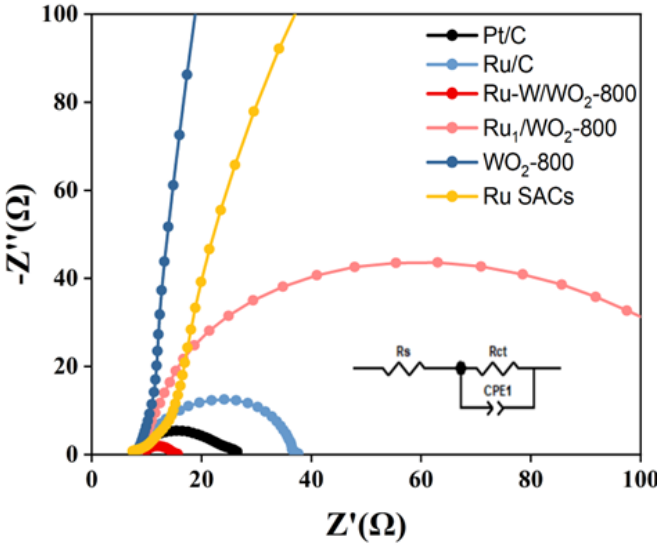

Figure S16. Nyquist plots of Ru-W/WO_2-800, Ru_1/WO_2-800, Pt/C, Ru/C, Ru SACs and WO_2-800.

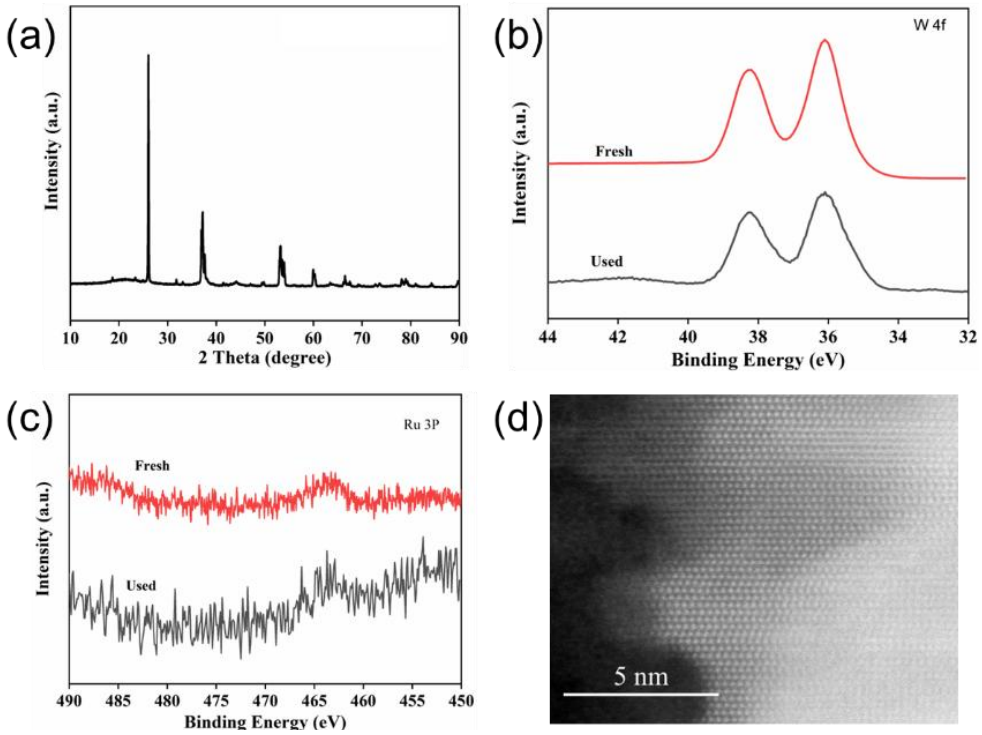

Figure S17. Physical characterization of Ru-W/WO2 after the long-term test. (a) XRD pattern. (b) W 4f XPS spectra. (c) Ru 3p XPS spectra. (d) HAADF-STEM image.

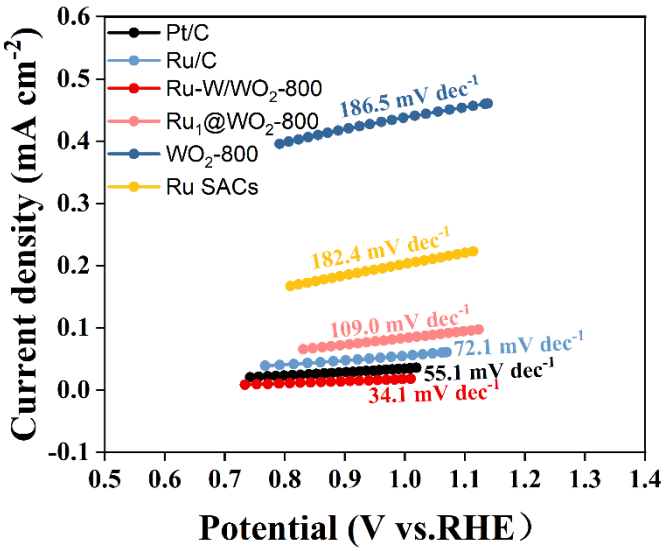

Figure S18. Tafel plots of Ru-W/WO_2-800, Ru_1/WO_2-800, Pt/C, Ru/C, Ru SACs and WO_2-800 in in alkaline simulated seawater of 1 M KOH and 0.5 M NaCl.

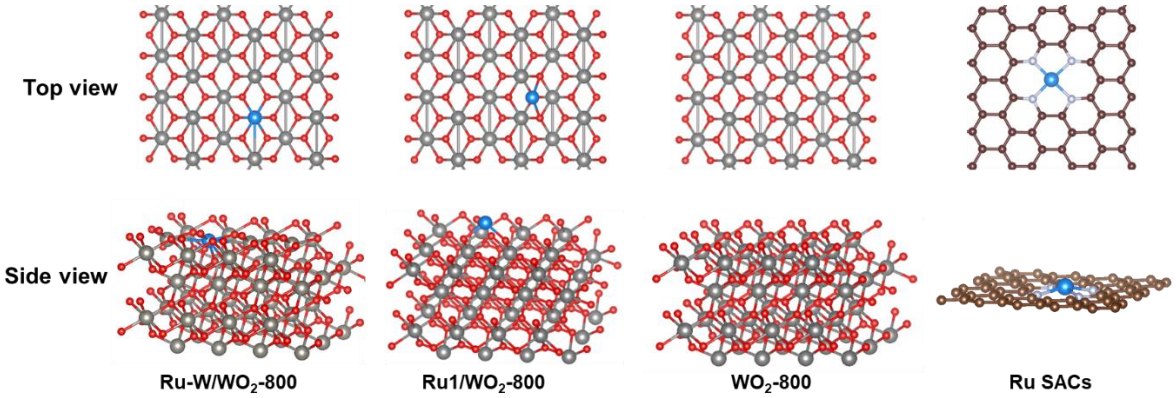

Figure S19. Simulative structures of Ru-W/WO_2-800, Ru_1/WO_2-800, WO_2-800, and Ru SACs.

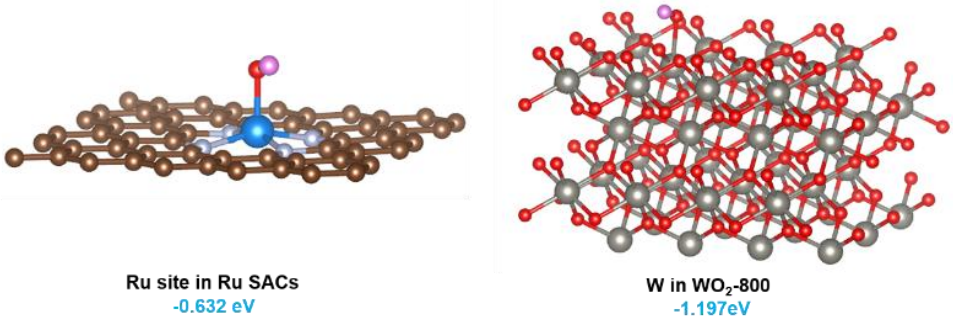

Figure S20. Simulative structure of OH adsorbed on the Ru SACs and WO_2-800 and the corresponding adsorption energy.

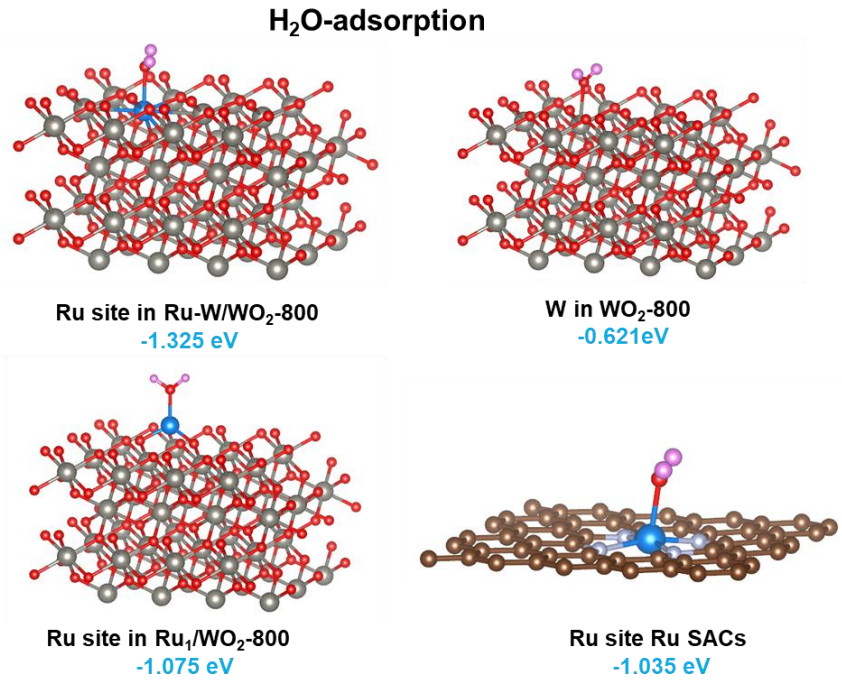

Figure S21. Simulative structures of H_2O adsorbed on Ru-W/WO_2-800, Ru_1/WO_2-800, WO_2-800 and Ru SACs and the corresponding adsorption energy.

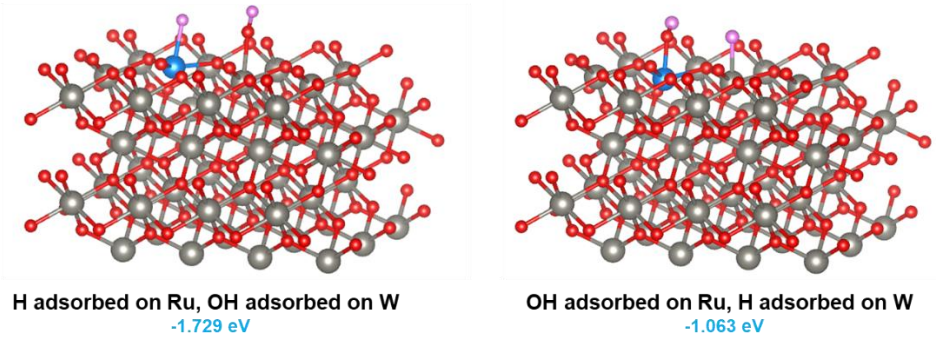

Figure S22. Different adsorption models and the corresponding adsorption energy of water dissociation intermediate (H-OH) on Ru-W/WO_2-800.

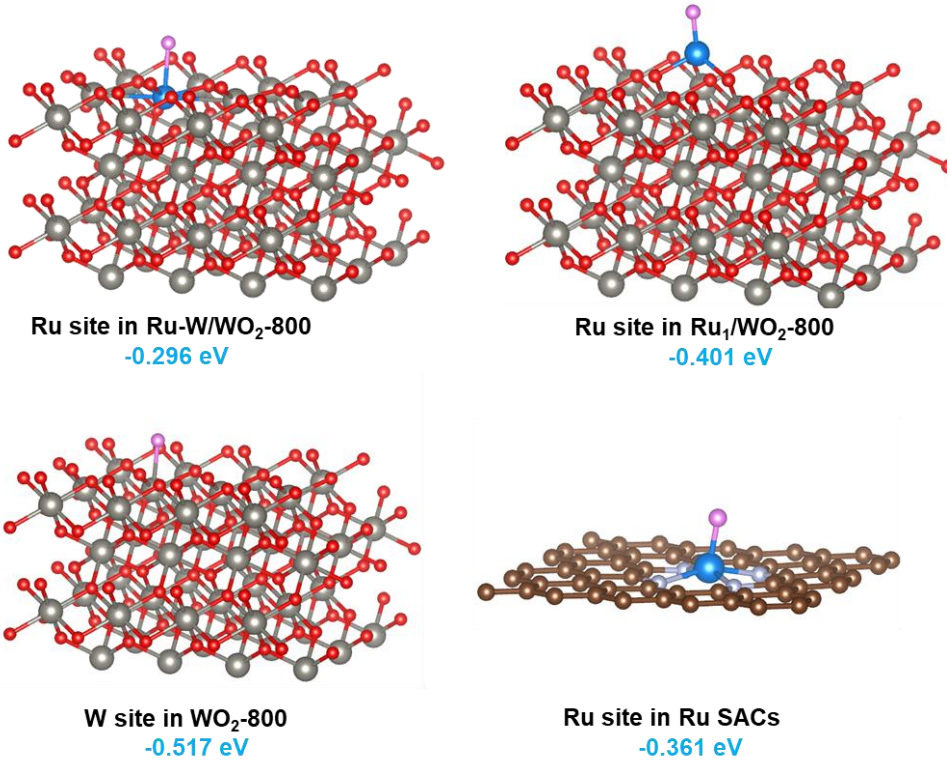

Figure S23. Simulative H adsorption model and corresponding adsorption energy on Ru and W sites

Supplementary Tables

Table S1. Metal content in various samples.

Sample	Metal content measured by ICP	
	Ru (wt%)	W (wt%)
Ru-W/WO_2-800	1.30	25.00
Ru_1/WO_2-800	1.27	25.77
Ru SACs	1.37	--

Table S2. EXAFS fitting parameters at the Ru K-edge for Ru-W/WO_2-800.

Sample	Shell	N[a]	R (Å) [b]	σ^2 (Å^2·10^{-3}) [c]	$\Delta E0$ (eV) [d]
Ru-W/WO_2-800	Ru-O	3.1±0.2	2.01±0.03	5.2±3.0	-1.1±0.2
	Ru-W	0.9±0.1	2.79±0.02	1.9±3.0	-2.3±0.2

[a] *N*: coordination numbers; [b] *R*: bond distance; [c] σ^2: Debye-Waller factors; [d] ΔE_0: the inner potential correction.

References

[1] G. Kresse,; J. Furthmüller, Comput. Mater. Sci. 1996, 6, 15−50.

[2] G. Kresse,; J. Furthmüller, Comput. Phys. Rev. B 1996, 54, 11169−11186.

[3] J. P. Perdew, K. Burke, Phys. Rev. Lett. 1996, 77, 38655−368.

[4] G. Kresse, D. Joubert, Phys. Rev. B 1999, 59, 1758-1775.

[5] P. E. Blöchl, Phys. Rev. B 1994, 50, 17953−17979.